
Ricci Curvature Based Volumetric Segmentation of the Auditory Ossicles.

Na Lei¹, Jisui Huang², Yuxue Ren^{3,*}, Emil Saucan⁴, Zhenchang Wang⁵,

Na Lei is with Key Laboratory for Ubiquitous Network and Service Software of Liaoning Province, Dalian University of Technology, Dalian, 116600 China (e-mail: nalei@dlut.edu.cn).

Jisui Huang is with Beijing Advanced Innovation Center for Imaging Theory and Technology, Capital Normal University, Beijing, 100084 China (e-mail: 2170502067@cnu.edu.cn).

Yuxue Ren (corresponding author) is with Beijing Advanced Innovation Center for Imaging Theory and Technology, Capital Normal University, Beijing, 100084 China (e-mail: snow_ren@foxmail.com).

Emil Saucan is with the Applied Mathematics Department, ORT Braude College of Engineering, Karmiel 2161002, Israel (e-mail: semil@braude.ac.il).

Zhenchang Wang is with Beijing Friendship Hospital, Capital Medical University, Beijing 100050, China (e-mail: cjr.wzhch@vip.163.com).

1 Abstract

The auditory ossicles that are located in the middle ear are the smallest bones in the human body. Their damage will result in hearing loss. It is therefore important to be able to automatically diagnose ossicles' diseases based on Computed Tomography (CT) 3D imaging. However CT images usually include the whole head area, which is much larger than the bones of interest, thus the localization of the ossicles, followed by segmentation, both play a significant role in automatic diagnosis. The commonly employed local segmentation methods require manually selected initial points, which is a highly time consuming process. We therefore propose a completely automatic method to locate the ossicles which requires neither templates, nor manual labels. It relies solely on the connective properties of the auditory ossicles themselves, and their relationship with the surrounding tissue fluid. For the segmentation task, we define a novel energy function and obtain the shape of the ossicles from the 3D CT image by minimizing this new energy. Compared to the state-of-the-art methods which usually use the gradient operator and some normalization terms, we propose to add a Ricci curvature term to the commonly employed energy function. We compare our proposed method with the state-of-the-art methods and show that the performance of discrete Forman-Ricci curvature is superior to the others.

2 Introduction

The auditory ossicles, situated in the middle ear, comprise the malleus, incus and stapes, which are the smallest bones in the human body. The function of the ossicles is to transmit sounds from the air to the cochlea and their damage produces hearing loss. It is therefore important to automatically diagnose ossicles disease. Computed

tomography (CT), which produces 3D image of areas inside the body, is an extensively employed and efficient technology for disease diagnosis. The ossicles localization followed by segmentation from 3D CT image play a significant role in automatically diagnose. Once the ossicles be segmented one can exactly construct surface triangular mesh for further analysis.

The 3D CT image for the auditory ossicles always includes the whole head area, which is pretty large compared to the small bones we consider. So the automatic localization of the ossicles can represent a labor saving progress relative to the currently employed method. On the other hand, the automatic segmentation of the ossicles can simplify the reconstruction of the ossicles' shapes, allowing for the easy comparison with that of the healthy ossicles. In general, location is a prerequisite for segmentation. The commonly employed local segmentation methods require manually selected initial points, rendering the procedure highly time consuming. To raise the automation level and help accurately segmenting the ossicles from the 3D CT image, we first propose a new method to locate the ossicles which requires neither template, nor manual labels. It relies on some of the connectivity properties of the auditory ossicles themselves and their relationship with the surrounding tissue fluid. Then we define a new energy function and segment the ossicles by minimize the energy. Most of the state-of-the-art methods use the gradient operator and some normalization terms. However, the widely adopted gradient operator only takes into account the first order derivative of the energy function. It is obviously that the second order derivative will provide more information. More precisely, curvature – i.e. the *shape operator* – represents the second derivative depending geometric tool that we shall prove efficient in the achievement of our proposed goal.

To this end we add a Ricci curvature [31] term to the energy function [37]. The energy function usually constructs a triangular grid according to the initial point to approximate the object, so the accuracy of the solution highly depends on the selection of the initial point. If there are too few initial points, it is difficult for the triangular mesh to approximate the original shape of the object. If there are too many initial points, it will consume too much labor. We use the localization of the ossicles position as the initial point of the local segmentation method. Since it is already a three-dimensional connected component, a natural mesh can be constructed based on the boundary. So we no longer need to guess the shape of the mesh based on a few initial points as before. We next proceed to the segmentation of the exact shape of the ossicles. Our results show that the Ricci curvature is indeed superior to the Original energy function method based on gradient operator in the localization and segmentation tasks at hand.

3 Related Work

3.1 3D Image Segmentation

Image segmentation is the most important step in medical imaging. There exists a vast amount of literature dedicated to segmentation algorithms. Here we only review some energy based methods which are related to our method. The use of deformable models for image segmentation has been pioneered by Kass et al. [15] with the introduction of the so called *snakes*: A snake is an energy-minimizing spline guided by external constraint forces and influenced by image forces that pull it toward features such as lines and edges. Terzopoulos et al. [32] expanded to three dimensions this approach which was initially used only in the two dimensional setting. In [7], Delingette introduced physically-based approach, resting on the geometry of simplicial meshes. McNerney and Terzopoulos [20] proposed a class of deformable models by formulating

deformable surfaces in terms of an affine cell image decomposition.

Level-sets were introduced by Osher and Sethian [23] and further popularized in computer vision and image analysis by Malladi et al. [19]. The level sets based method has the ability of splitting freely to represent each object when the considered image contains more than one object of interest. Leventon et al. [16] extended the original energy by introducing a representation for deformable shapes and defining a probability distribution over the variances of a set of training shapes. A frequent criticism of this approach is that the signed distance function which the shape model assumes, does not form a linear space, which can lead to the generation of irregular shapes if the shape of the studied object changes abruptly. Nevertheless, the approach quickly became popular and was extended in several directions, among others by Tsai et al. [33] who employed Leventon's modeling method with a region-based energy functional. Pohl et al. [26] utilized LogOdds to obtain a shape representation that encodes the shape of an anatomical structure as well as the variations within, in a manner suited for medical imaging. Recently, Chen et al. [37] presented a 3D selective segmentation model which is inherently suited for efficient implementation.

3.2 Ricci Curvature

Curvature plays an important role in geometry since it represents a measure to quantify the deviation of a geometrical object from being intuitively flat. Amongst the various, classical existing types of curvature, sectional curvature is the most expressive one, and as such it has which has wide range of practical applications, in particular in complex networks. In particular, Eckmann et al. [8] used curvature to define a World Wide Web landscape whose connected regions of high curvature characterize a common topic. Shavitt et al. [30] used curvature called internet geometric curvature to captures the property of Internet. Saucan and Appleboim [28] introduced a new clustering method for vertex- and edge-weighted networks which is based upon a generalization of the combinatorial curvature.

Ricci curvature is a more abstract and less intuitive concept. It became widely known to larger audiences, beyond the circle of differential geometers, after Perelman's seminal work on the Ricci flow [24, 25], and its consequent use in solving the Poincaré Conjecture. Spurred partly by the renewed interest in the Ricci flow, Chow and Luo [5] showed that the circle-packing based combinatorial analogue of Hamilton's Ricci flow for surfaces [13], behaves similarly to the classical one.

This approach proved to be extremely malleable and useful in a variety of applications in graphics, imaging and complex networks, as demonstrated by the work of Gu et al. [10, 12, 14, 38]. A quite different and elegant approach to discretize the Ricci curvature, in particular to networks, is due to Ollivier [22]. However, by its very definition it requires solving an optimal transport problem that reduced to a linear programming problem, which renders computations slow and laborious, especially on large scale networks. Yet another viewpoint towards the discretization of Ricci curvature, based upon the connection between curvature and the Laplacian operator, was adopted by Forman [9]. Forman's method applies to weighted cell complexes and it was adapted to the case of undirected (as well as directed) networks by Sreejith et al. [31]. It is this last type of Ricci curvature that we make appeal to in the present paper, due to its simplicity and effectiveness in computations, even on very large scale CT image.

4 Discrete Ricci Curvature

We begin by briefly recalling the classical definition of Ricci curvature of smooth manifolds (for further details see, e.g. [3]).

Suppose that (M, g) is an n -dimensional Riemannian manifold, let p be a point in M , let $T_p M$ denote the tangent space of M at a point p , and let $\zeta, \xi, \eta \in T_p M$. Define $g : T_p M \times T_p M \times T_p(M) \rightarrow T_p M$, as $g(\zeta, \eta, \xi) = R(\zeta, \eta)\xi$, where R denotes the *Riemannian curvature tensor*. (For further details on these and

Then the *Ricci curvature tensor* at p Ric_p is the bilinear map $\text{Ric}_p : T_p M \times T_p M \rightarrow \mathbb{R}$ define as:

$$\text{Ric}_p(\xi, \eta) = \text{trace}(g) ; \quad (1)$$

for any $\xi, \eta \in T_p M \times T_p M$. If ξ is unit tangent vector, Ricci curvature of ξ , $\text{Ric}(\xi)$ is defined naturally as follows:

$$\text{Ric}(\xi) = \text{Ric}(\xi, \xi) . \quad (2)$$

If $\{e_i\}_{i=1}^n$ is an orthonormal basis of $T_p M$, then the *scalar curvature* (at p) is defined as the average of the Ricci curvatures of the basis elements, that is

$$\text{scal}(p) = \frac{1}{n} \sum_{i=1}^n \text{Ric}(e_i) . \quad (3)$$

Note that Ricci curvature is a tensorial measure, attached to a direction, while the scalar curvature is (as the name stands to wit), as a scalar measure, attached to a point. (For further details on the Riemannian geometry notions introduced above see, e.g. [3].)

While the tensorial approach to Ricci curvature presented above is important in classical Riemannian geometry as well as in its applications to generalized relativity and cosmology, data arising in computer related applications, and in particular in medical imaging, is discrete (obtained, usually, by sampling of the analogous signal/image). In consequence, a discrete version of Ricci curvature is required.

The discrete Forman-Ricci curvature, as it was extended and adapted to undirected graphs in [9], is an *edge-based measure* defined as follows:

$$F(e) = w_e \left(\frac{w_{x_1}}{w_e} + \frac{w_{x_2}}{w_e} - \sum_{e_{x_1} \sim e, e_{x_2} \sim e} \left(\frac{w_{x_1}}{\sqrt{w_e w_{e_{x_1}}}} + \frac{w_{x_2}}{\sqrt{w_e w_{e_{x_2}}}} \right) \right) \quad (4)$$

(See Figure 1.)

- e denotes the edge under consideration between two nodes x_1 and x_2 .
- w_e denotes the weight of the edge e under consideration.
- w_{x_1} and w_{x_2} denote the weights associated with the nodes x_1 and x_2 , respectively.
- $e_{x_1} \sim x_1$ and $e_{x_2} \sim x_2$ denote the set of edges incident with nodes x_1 and x_2 , respectively, after excluding the edge $e = (x_1, x_2)$ under consideration.

We work with the standard model for 3D CT image, where each voxel is viewed as a (small) cube, thus the 3D picture is viewed as cube lattice. The graph we consider is the dual graph of this lattice, i.e. each node represents the center of a cube (voxel), and an edge connects adjacent voxels (cubes), where adjacency is along faces only.

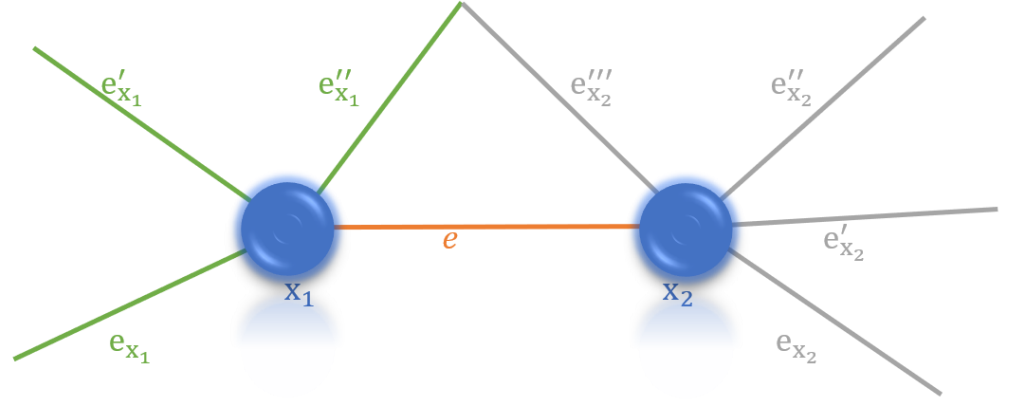


Figure 1. The elements appearing in the Forman's curvature of an edge.

Thus each node has six incident edges except the boundary nodes. The gray value of a CT node x can be regarded as w_x and w_e be calculated by equation:

$$w_e = \exp(|w_{x_1} - w_{x_2}|) \quad (5)$$

where x_1 and x_2 are nodes incident with edge e .

A discrete definition of the scalar curvature of a node (which is frequently named in the literature as the Ricci curvature of a node) can also be defined in a similar manner to the one in the classical case introduced in Formula (3) above:

$$F(x) = \frac{1}{\deg(x)} \sum_{e_x \sim x} F(e_x) ; \quad (6)$$

where e_x denotes the edges incident with the node x and $\deg(x)$ denotes (as usually) the total number of e_x .

5 Acquisition of initial point

We mainly use the connectivity to obtain connected component of ossicles. The proposed method is suitable for any scaling, rotation and affine transforms, and it is also designed to fit the abnormal ossicles.

5.1 Concepts and Notation

We begin by introducing some concepts and notations that will be used in locating the ossicles. Also, before proceeding, let us note that the 2D domain we discuss below is usually one slice of the entire 3D CT image.

- **Path:** In section 4 we have explained 3D CT image in geometric view: each node has six incident edges (except the boundary nodes) in the dual graph, each node has four incident edges (except the boundary nodes) in 2D, i.e. a slice of the 3D CT image, if restricting graph to this slice. By *path* we mean a continuous function from $[0, 1]$ to edges.

We define the following sets:

- If x is a node, D is a set of nodes, let $P_D^i(x)$ be defined as

$$P_D^i(x) = \{ y \mid \exists i\text{-dimensional path from node } x \text{ to node } y, \text{ i. e. all nodes on path except } x \text{ belong to } D; \} \quad (7)$$

where by a i -dimensional path we mean a path in 2D or 3D Euclidean space (a path in 1D is trivial). Figure 2 is a $5 \times 4 \times 3$ image. The node having 0 value is x_0 (there is only one such node), nodes having 1 value form the set D_1 , and nodes having 3 value the set D_3 . Then $P_{D_1}^2(x_0)$ are the red nodes and $P_{D_3}^3(x_0)$ are green nodes.

- If A is a set of nodes

$$P_D^i(A) = \bigcup_{x \in A} P_D^i(x) \quad (8)$$

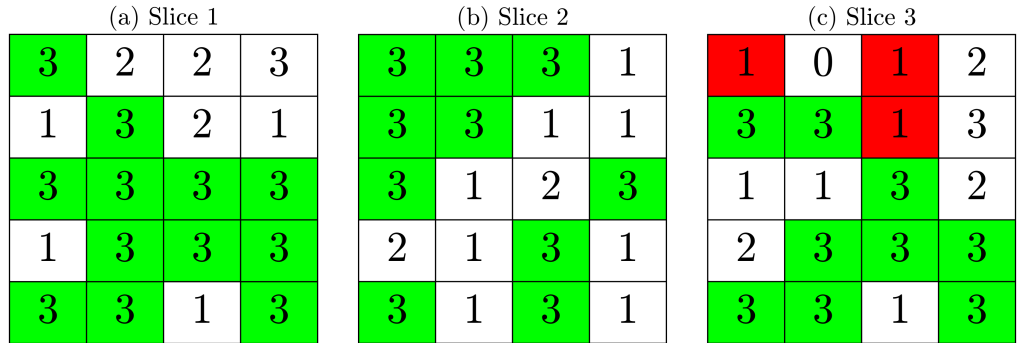


Figure 2. Illustration of the P_D^i notation: The unique node having 0 value is x_0 , D_1 denotes nodes having 1 and D_3 nodes having 3. $P_{D_1}^2(x_0)$ are the red nodes and $P_{D_3}^3(x_0)$ are green nodes.

The 3D CT image considered consist of three components: air, tissue fluid and bone which are rendered, according to their density, as black, gray and white respectively. Let Ω_1 , Ω_2 , Ω_3 represent 3D connected component of bone, tissue and air, respectively. Thus $\Omega_1 + \Omega_2 + \Omega_3 = \Omega$. We next define background and foreground based on previous definition, as follows:

- **Background B :** Background is defined as the set : $B = P_{\Omega_3}^3(a)$, where a is a point in the outside air area, which are nodes beyond 3D convex hull of the skull. This implies that background is a subset of Ω_3 .

- **Foreground F :** This is defined, naturally, as the complementary domain of the background, i.e. $F = \Omega - B$. Note that the foreground will also contain some air areas which are not connected with outside air.

5.2 Coarse Localization

Since the whole 3D CT image is too large to allow efficient computations, we first roughly localize the ossicles by determining the centroid of skull. This is easy to achieve since the skull is the largest three-dimensional connected bone in the entire CT image. We next calculate the centroid and determine the 3D cubic domain surrounding the ossicles based on empirical observation and physician’s experience. The obtained cubic area here is only a first, coarse approximation, since it is needed only to reduce the volume of further computations. We denote this area by Ω . It implies all slices of 3D image have a common rectangular domain.

Figure 3 shows left and right cubic domain in one slice of 3D image, while Figure 4 is another slice of only right cubic domain. We apply all the operations that will be introduced in the sequel to both cubic domains independently, though we only explicate operations in right cubic domain, i.e. right ossicles.

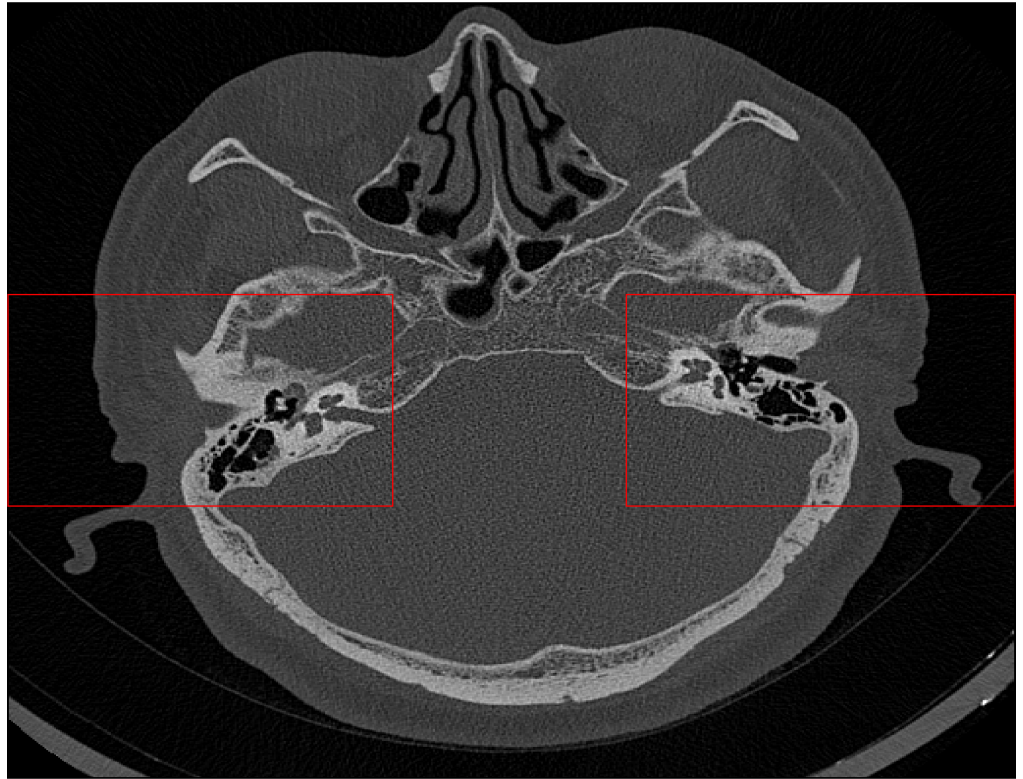


Figure 3. Left and right cubic domains in one slice of the 3D image.

5.3 Properties of Normal Ossicles

5.3.1 Anatomical property

The normal ossicles are suspended by ligaments in the middle ear. Since the gray values of ligaments and bones are significantly different, the ossicles appear as if floating in the auditory meatus, i.e. they are completely isolate bones. Using this property in a manner that will be described in detail in Section 5.4, we shall obtain a set including the three-dimensional connected bone component containing the ossicles.

5.3.2 Property based on 3D image

By using the above property we can get a set of 3D connected bone component containing ossicles. The following property produces a significant criterion for the identification of the ossicles from it.

We begin by noting that the foreground in which ossicles are located is isolated by background in two dimensions. Figure 4 shows an illustrative 2D CT image, where the red color demonstrates one 2D slice of the three-dimensional ossicles. As we can see, there is a very thin layer of tissue around the red bone, some air is surrounding these tissue and there is a 3D path between these air and outside air (the existence of 3D

path can not be observed in one single 2D slice). Thus, it would appear as if the foreground floats in background.



Figure 4. Properties of normal ossicles based on 3D image: White part area represents the foreground, black part the background. The ossicles are located in the red domain which is actually contained in foreground. Therefore, the black domain around it can in fact connect to the outside air, a phenomenon that not observable in this slice, as this part of foreground does not connect to the image border included in $\partial\Omega$.

We further elaborate on the ossicles' location aspect mentioned above, by using the notation introduced in Section 5.1: Denote by $O \subset \Omega_1$ one 3D bone connected component locate in k layers of slices, and let O_j , $1 \leq j \leq k$ be the j -th 2D slices of O . For example, if O exists on slices from the 50-th slice to the 65-th one, O_1 is the set of all the nodes of O belong to the 50-th slice, and O_{10} the set of all the nodes of O belong to the 59-th slice. It is worth noting that O_j may by definition have many 2D connected components in one slice. Then the 3D bone connected component O includes ossicles if and only if

$$\text{There exists a } j \text{ such that } O_j \not\subset P_F^2(\partial\Omega) \quad (9)$$

This property only suitable for normal case (we refer to it as Case 1 in Section 5.5). The abnormal cases can be converted to normal case, discussed in Section 5.5.

5.4 Connected Bone Component

We compute all the 3D connected components of bones in one of the cubic domains considered above. As introduced in Section 5.3.1, the normal ossicles are suspended by ligaments in the middle ear. But some abnormal ossicles may be connected to the surrounding components. So we perform an eroding operation on the bones to help us to detect the set of 3D bone connected components contains ossicles. Note that at this stage it is not necessary to ensure that the obtained components capture the precise shape of the bones, because this preliminary stage is solely for determining the location. Once we have identified the ossicles, we can accurately determine the shape using the method described in Section 6.

5.5 Different Situations in Location

We have obtained the cubic domain Ω representing the 3D CT image under investigation, and the bone connected component Ω_1 . Let Ω_2 , Ω_3 denote the tissue and the air domains, respectively. $\Omega_1 + \Omega_2 + \Omega_3 = \Omega$. Let $a \in \Omega_3$ represents a point in the outside air, i.e. beyond the convex hull of skull.

Case 1: Normal Ossicles

If the ossicles are normal, they can be located through the property described in Section 5.3.2 above. The background is, conform the convention established in the previous section, $B_1 = P_{\Omega_3}^3(a)$, and foreground is, naturally, $F_1 = \Omega - B_1$. Then it is possible to locate the ossicles using condition (9).

If the ossicles can not be located using the method described in Case 1, then it indicates that there exists a tissue blockage between the outer ear and the ossicles (cf. Case 2 below), or the tissue fluid connected component where the ossicles are located is connected to the other tissue fluid (Case 3), or both cases (Case 4).

Case 2: Non-smooth External auditory canal

Denote $D_1 = \{x | d(x, B_1) < r, x \in \Omega_2\} \cup B_1$. Then, due to the thin tissue blockage appearing in the neighborhood of B_1 , the following inequality obviously holds: $\text{Vol}(P_{\Omega_3}^3(D_1)) > \text{Vol}(D_1)$. The external area may still be connected to the middle ear as long as this blockage has been removed. It follows that in this case the background expands: $B_2 = P_{\Omega_3}^3(D_1)$. Therefore $F_2 = \Omega - B_2$ represents, in this case, the foreground.

As shown in Figure 5(a), the outer ear and middle ear are separated by a thin tissue, so that the outer ear does not communicate directly with the middle ear. In fact, in the entire 3D CT image, this tissue spans many partial 2D images, resulting in the outer ear being unable to connect to the middle ear in the resulting image. The red area in Figure 5(b) indicates the area to which the air from the exterior can reach, i.e. a slice of B_1 . Intuitively, we only need to erase this thin tissue, and the red area can continue to connect to the middle ear.

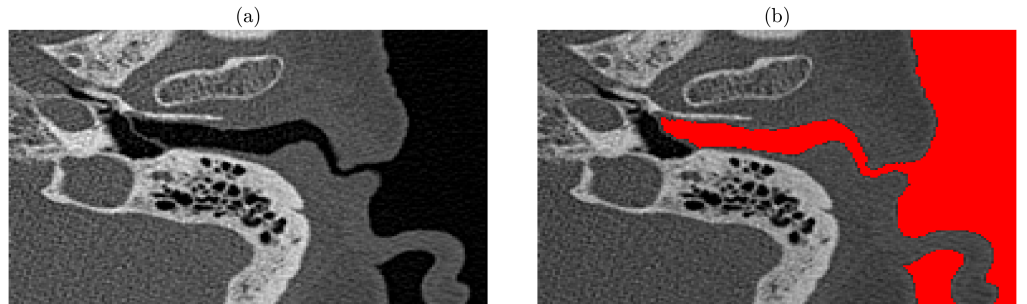


Figure 5. Non-smooth external auditory canal in Case 2: Figure 5(a) is a CT image in Case 2. There is a blockage between the outer ear and the middle ear which prevents the red part in 5(b) (air domain connected to outside of skull) from connecting to middle ear.

Case 3: Middle ear abnormal density shadow

In this case the background can reach middle ear and, moreover, the foreground will be connected to $\partial\Omega$. Figure 6(a) illustrates the case in which foreground, containing ossicles (in red), is connected to $\partial\Omega$. We can remove this connectivity by erasing some tissue around ossicles, i.e. by expanding the background B_1 in Case 1. Thus $B_3 = \{x | d(x, B_1) < r, x \in \Omega_2\} \cup B_1$, $F_3 = \Omega - B_3$. As shown in Figure 6(b), some of the slices of foreground containing ossicles are isolated.

Case 4: Middle ear abnormal density shadow and non-smooth external auditory canal

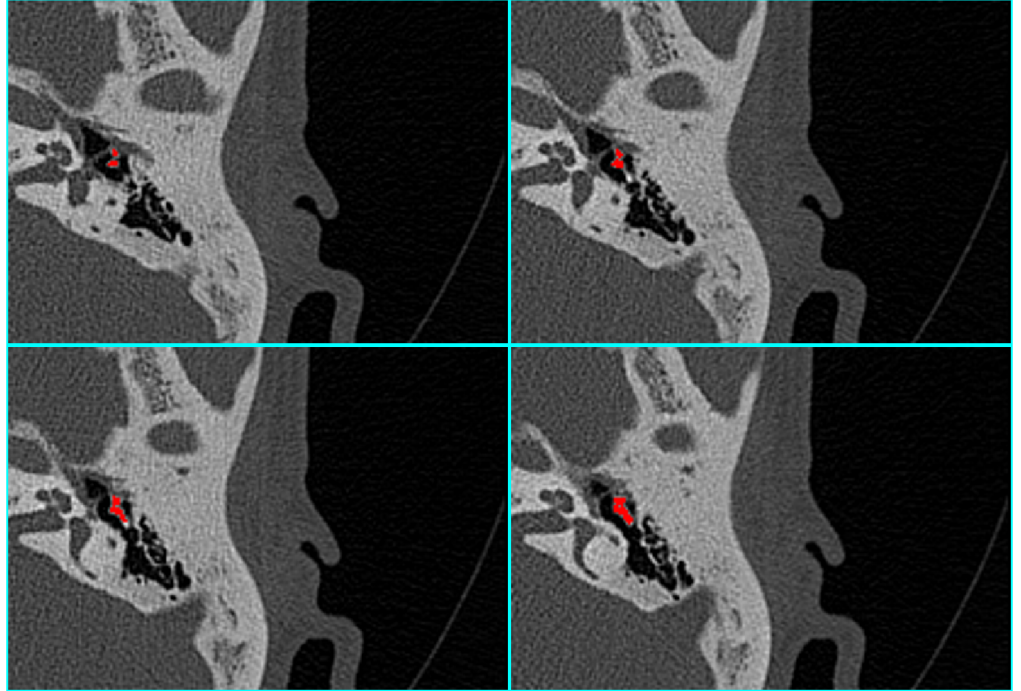
Clearly, this case represents a combination of Case 2 and Case 3. This means there is a tissue blockage between the outer ear and the ossicles (Case 2) and the tissue fluid connected component in which the ossicles are located is connected to the other tissue fluid (Case 3).

We begin by expanding the background to middle ear using method detailed in Case 2. Next we erase part of tissue near the ossicles, by using the method described in Case 3. Denote: $D_2 = D_1 - B_1$, $D_3 = B_2 - D_2$, $B_4 = \{x | d(x, D_3) < r, x \in \Omega_2\} \cup D_3$, and put $F_4 = \Omega - B_4$.

Case 5: External auditory canal obstacle

Intuitively, the external auditory canal is the jutting strongly concave domain on the

(a)



(b)

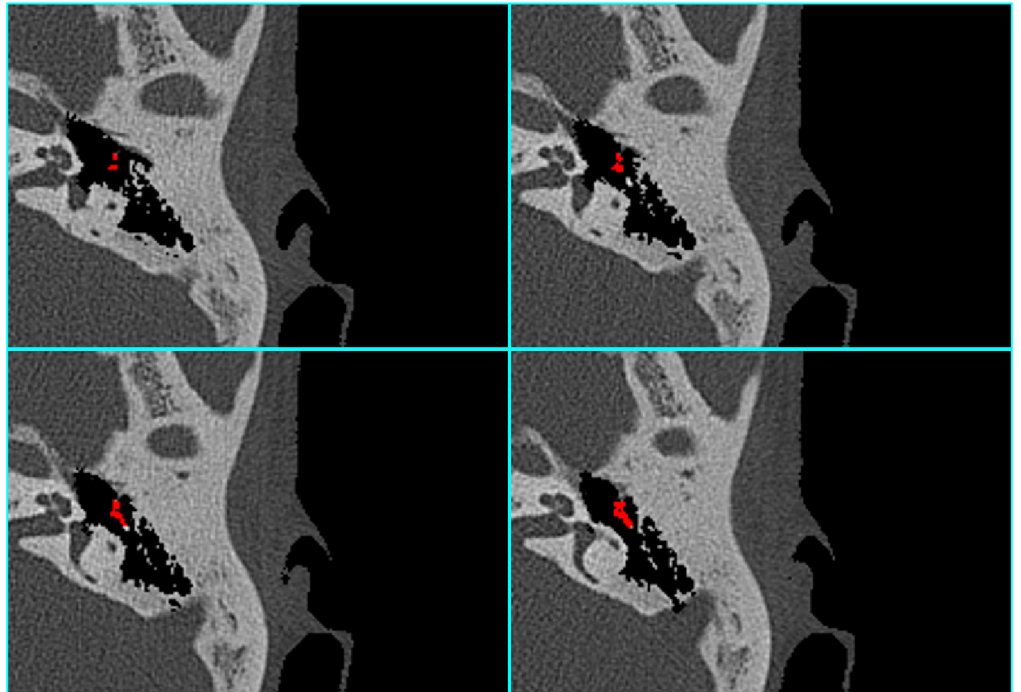


Figure 6. Middle ear abnormal density shadow: In Figure 6(a), all the slices of the foreground containing red ossicles connect to image border in 2D. In Figure 6(b), some foreground slices are isolated after removing some tissue around ossicles.

bone of skull in cubical area. So we use some morphological operation to depict this intuition. Figure 7 shows skull dilated by the kernel K_1 :

$$K_{1_{ijk}} = 1; 1 \leq i, j, k \leq 9. \quad (10)$$

Start observing from the last slice, the external auditory canal E_1 is concave increasingly.

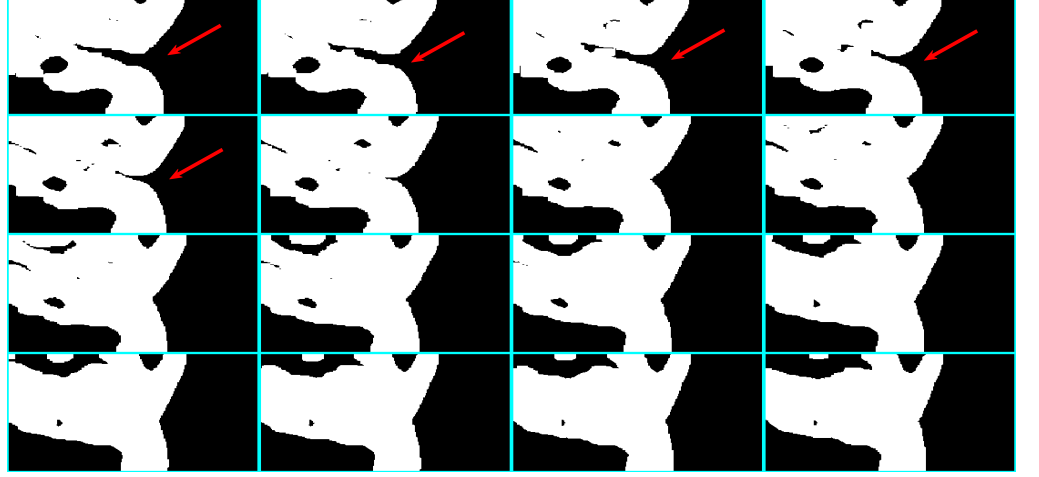


Figure 7. Skull image dilated by kernel K_1 : The increasingly concave domain represents the location of outer ear.

E_1 is actually smaller than the actual size of external auditory canal, because dilating operation will increase area of bone and consequently decrease area of air. We next determine more accurate shape of the outer ear and middle ear E_2 with smaller kernel K_2 , by extending E_1 inward, where

$$K_{2_{ijk}} = 1, 1 \leq i, j, k \leq 7; \quad (11)$$

$E_1 \subset E_2$. Similarly, we use a smaller morphological kernel K_3 :

$$K_{3_{ijk}} = 1, 1 \leq i, j, k \leq 5; \quad (12)$$

to extend E_2 inward in the dilated image using kernel K_3 , thus obtaining the domain E_3 . Note that $E_2 \subset E_3$. We next define E :

$$E = E_3 \oplus K_3; \quad (13)$$

where \oplus denotes *morphologically dilation* [11]. In Figure 8(a), we can see that the outer ear is completely filled with tissue fluid. In Figure 8(b), the red area represents $E_1 \oplus K_1$, the red or green area represents $E_2 \oplus K_2$, and red, green or blue area indicates $E_3 \oplus K_3$, i.e. E . This color area is actually the domain of outer ear and middle ear. The ossicles are beneath the E domain, it will appear in a little box area in 8(a). So we can expand E domain downward - this is also a parameter determined by experiments. Then we can obtain all the 3D bone connected components with a 3D path between them and expanded E .

From Case 1 to Case 4, we employed the method in 5.4 to obtain connected bone in all the cubic domain (Ω). We thus obtain a set of bones around the domain of the auditory canal, which is a much smaller set containing the ossicles. We will use this new bone set and directly set the background as Ω_3 , i.e. $B_5 = \Omega_3$, $F_5 = \Omega - B_5$.

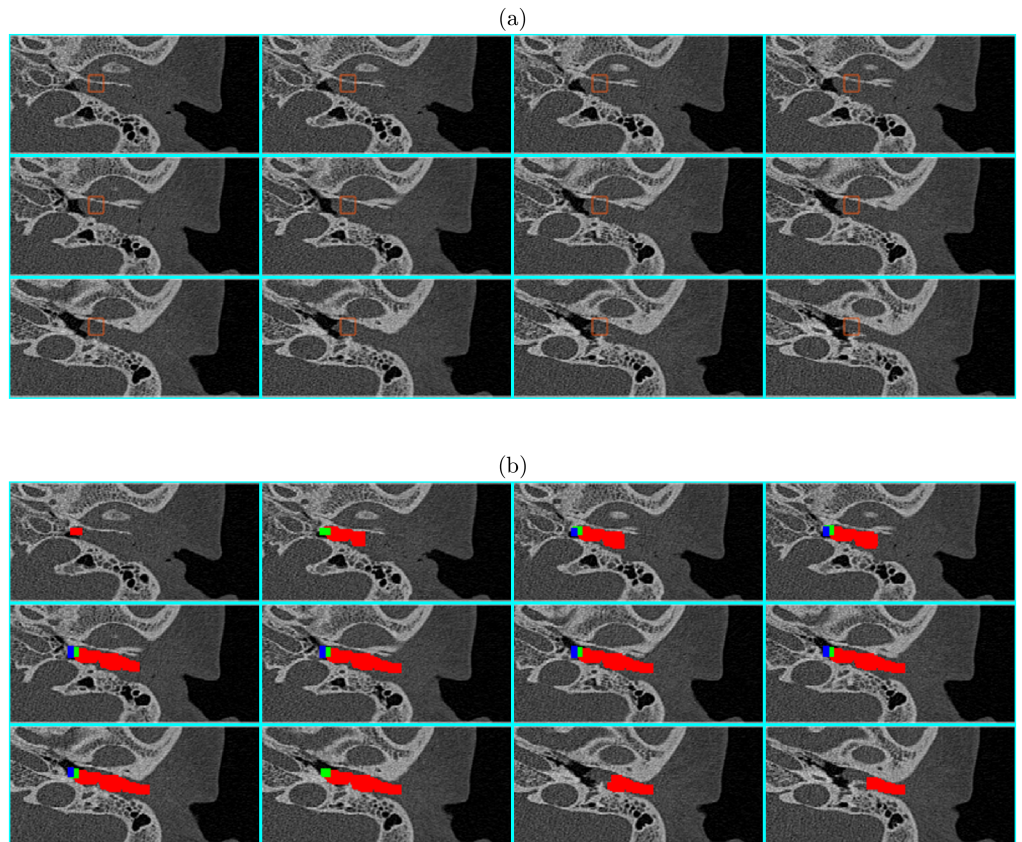


Figure 8. External auditory canal obstacle: External auditory canal is filled with tissue fluid in Figure 8(a); the box therein represents the position where ossicles will appear. In Figure 8(b) the red domain is the auditory canal determined using the biggest morphological kernel, i.e. K_1 . Similarly, green and blue represent the domains determined using K_2 and K_3 respectively.

6 Segmentation

6.1 Energy Function

In this section we introduce our novel method for the volumetric segmentation of the ossicles. The level set method [23] [37] is a classical segmentation method. It minimizes an energy function to get the object boundary. This method needs an initial approximation of the boundary and the accuracy is highly related to it. Here we use the coarse approximation of ossicles obtained in the previous section as the initialization. We redefine the energy function by adding a new item which is based on Ricci curvature, in a manner that is also inspired by the elegant framework introduced by Mumford and Sha in their classical paper [21].

Given a two-dimensional close surface Γ which can be embedded in $\Omega \subset \mathbf{R}^3$, and a function $f(x)$ on Ω (here in our problem $f(x)$ is the gray value of voxel x). We define the energy function $E(\Gamma)$ as follows:

$$\min_{\Gamma} E(\Gamma) = \alpha E_G(\Gamma) + E_F(\Gamma). \quad (14)$$

where

$$E_G(\Gamma) = \int_{\Gamma} G(x) ds, \quad (15)$$

where $G(x)$ denotes the discrete Ricci curvature (6) of the node (pixel value) given by the intensity function $f(x)$, instead of the common edge detector (see discussion above).

$$E_F(\Gamma) = \lambda_1 D_f(S_1) + \lambda_2 D_f(S_2) \quad (16)$$

where $D_f(S_i)$ represents the variance of $f(x)$ in domain S_i ; S_1 is the domain within Γ and with distance to boundary Γ less than a given threshold γ^{in} , and similarly, S_2 is the domain outside Γ with distance to boundary Γ less than another preestablished threshold γ^{out} .

Let $\phi(x)$ represent the distance from point $x \in \mathbf{R}^3$ to the close surface Γ . Then $\phi(x)$ is positive if x is inside Γ , and negative if x is outside it. Therefore

$$\begin{aligned} E(\Gamma) &= \alpha \int_{\Omega} G(\mathbf{x}) \nabla(H(\phi)) d\mathbf{x} \\ &+ \lambda_1 \int_{\Omega} \chi_1(\phi) (f(x) - E(S_1))^2 d\mathbf{x} \\ &+ \lambda_2 \int_{\Omega} \chi_2(\phi) (f(x) - E(S_2))^2 d\mathbf{x} \end{aligned} \quad (17)$$

where $E(S_1)$, $E(S_2)$ denote the mean energy of S_1 , S_2 , respectively. Next we derive the Euler-Lagrange Equation (14), containing $\delta(\phi)$, $\delta(\phi - \gamma_{in})$, $\delta(\phi + \gamma_{out})$. However, it is worth firstly pointing out that since we have assumed that $\phi(x)$ is a distance function from point x to the boundary Γ , in other words, $\Gamma = \{x | x \in \Omega, \phi(x) = 0\}$. In principle, once Γ is chosen, the value of $\phi(x)$ at any point $x \in \Omega$ can be determined. Therefore we need only to compute $\phi^{-1}(0)$. So we consider the item containing $\delta(\phi)$:

$$\begin{aligned} \delta(\phi) &\left(\alpha \nabla \cdot \left(\frac{G(\mathbf{x}) \nabla \phi}{|\nabla \phi|} \right) \right. \\ &+ \lambda_2 (f(\mathbf{x}) - E(S_2))^2 \\ &\left. - \lambda_1 (f(\mathbf{x}) - E(S_1))^2 \right) = 0 \end{aligned} \quad (18)$$

Note that we assume ϕ is a distance function which does not influence directly the Euler-Lagrange Equation (18). There exist two accepted manners of elimination this limitation of distance function. The first is adding this penalty to $E(\Gamma)$, thus introducing the gradient descent term of the Euler-Lagrange equation into the iterative

formula of the level set method [17]. The second is to iterate ϕ without any restrictions and re-initialize it after each iteration to restore the signed distance property. The first method is more intuitive and apparently efficient. However, the total number of volume occupied by the ossicles is approximately only 200 voxels. Therefore, a little fluctuation of distance function will result in huge error. Numeric experiments show that the first method has some fluctuation especially around $\phi^{-1}(0)$. The error introduced by this method is not obvious for big objects such as the whole brain, but it affects significantly results obtained on small object such as the ossicles. This conducts us to adopt the second method. To this end we make appeal to a multigrid method [1] which needs to solve this question in a coarser grid for this purpose. But it is worth noting that the ossicles are very small (approximate 200 voxels) so we cannot implement any formula on the coarser grid. In consequence, we use gradient descent to iterate. During the re-initialization process we use the specific initialization method which described in Section 6.2.

6.2 Re-initialization and Narrow Band

The distance function $\phi(x)$ has the following property:

$$\begin{aligned} |\nabla\phi(x)| &= 1, \text{ for } x \in \Omega \subset R^n ; \\ \phi(x) &= q(x), \text{ for } x \in \partial\Omega. \end{aligned} \tag{19}$$

We use fast marching method [2,34] to calculate the distance function, method in [4] to update grid value and binary heap method to maximize the speed of this algorithm.

Note that our aim is to locate the boundary, i.e. the set $\phi^{-1}(0)$, thus we only need to focus on the values around it. Therefore, when the algorithm is running, the fast marching algorithm can be terminated when the obtained distance is greater than a certain value γ . Given the nature of the algorithm, it is easy to see that by stopping the computation when the distance is greater than γ , we actually calculate all the points x such that $|\phi(x)| < \gamma$. Therefore, it follows that we can implement the gradient descent method only around $\phi^{-1}(0)$.

7 Algorithm

In this subsection we give three algorithms. Algorithm 1 is used to localize the ossicles in a bone connected component if they are included in this component. Algorithm 2 is used to deal with the 5 cases we discussed in section 5.5. Algorithm 3 is our main algorithm, which outputs the 3D surface of the ossicles.

Algorithm 1 Localization

Input: bone Ω_1 , background B , foreground F

Output: ossicles

```

1: for 3D connected component  $O \in \Omega_1$  do
2:   if  $O$  conforms to equation (9) then
3:     return  $O$ 
4:   end if
5: end for
6: return  $\emptyset$ 

```

Algorithm 2 SearchingOssicles

Input: cubic domain Ω

Output: ossicles

- 1: Calculate 3D bone connected component Ω_1 using method in section 5.4
- 2: Calculate Ω_2, Ω_3 using global threshold method such that $\Omega_1 + \Omega_2 + \Omega_3 = \Omega$
- 3: Calculate a point in outside air area beyond the convex hull of skull
- 4: $a = \text{Localization}(\Omega_1, B_1, F_1)$
- 5: **if** $a \neq \emptyset$ **then**
- 6: **return** a
- 7: **end if**
- 8: $D_1 = \{x | d(x, B_1) < r, x \in \Omega_2\} \cup B_1$
- 9: **if** $\text{Vo}(P_{\Omega_3}^3(D_1)) == \text{Vo}(D_1)$ **then**
- 10: $a = \text{Localization}(\Omega_1, B_3, F_3)$
- 11: **if** $a \neq \emptyset$ **then**
- 12: **return** a
- 13: **end if**
- 14: **end if**
- 15: $a = \text{Localization}(\Omega_1, B_2, F_2)$
- 16: **if** $a \neq \emptyset$ **then**
- 17: **return** a
- 18: **end if**
- 19: $a = \text{Localization}(\Omega_1, B_4, F_4)$
- 20: **if** $a \neq \emptyset$ **then**
- 21: **return** a
- 22: **end if**
- 23: calculate bone Ω_1 , foreground F_5 , background B_5 using method in case 5
- 24: $a = \text{Localization}(\Omega_1, B_5, F_5)$
- 25: **if** $a \neq \emptyset$ **then**
- 26: **return** a
- 27: **end if**
- 28: **return** \emptyset

8 Experiments

The data used in our experiments is courtesy of the Beijing Friendship Hospital and consists of 100 CT images. After determining the location of ossicles, we depict, in Figure 9, the 3D CT image of the region surrounding them. Next we recover the 3D shape by minimizing the energy function (14) proposed in this paper. During this process we set $\gamma = 2$. The thresholds γ^{in} and γ^{out} are used to calculate $E(S_1)$ and $E(S_2)$, respectively. However, for the ossicles, we can add some of the prior knowledge, namely the fact that the inside of the ossicles is white (bone) and the outside is black (air). Therefore, we set $E(S_1) = 1$ and $E(S_2) = 0$. The numerical experiment result shows that this represents a highly efficient method for ossicles, even for those surrounded by large amounts of tissue fluid.

In most previous works the function $G(x)$ in equation 15 is defined as the gradient operator, but not the Ricci curvature operator:

$$G(x) = \frac{1}{1 + |\nabla G_\sigma * f(x)|^2} \quad (20)$$

where G_σ is a Gaussian kernel with standard deviation. However, in our setting this method does not perform sufficiently well. In Figure (10) we show the segmentation

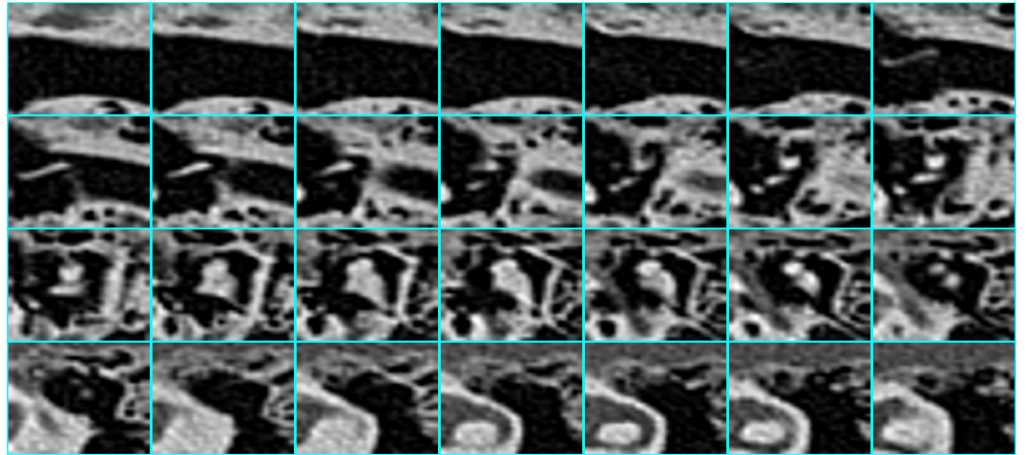


Figure 9. 3D CT image of the region surrounding the ossicles.

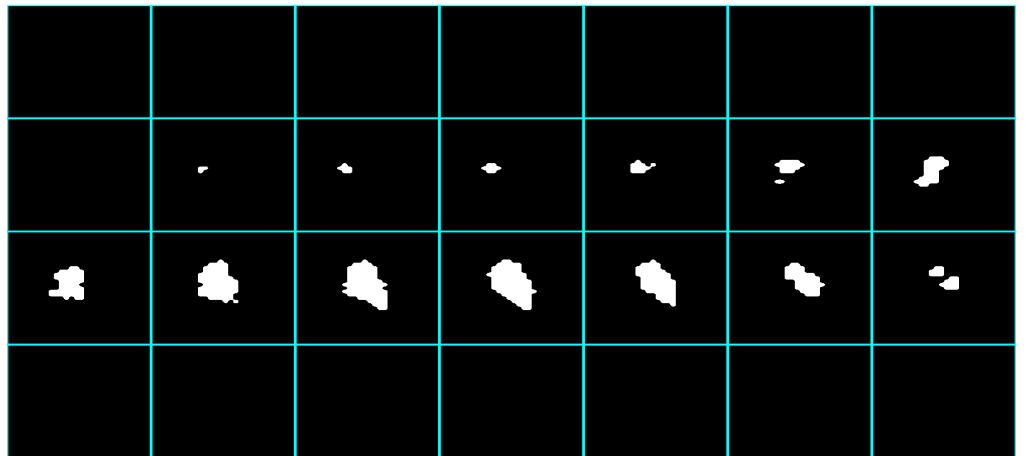


Figure 10. Segmentation result obtained using the gradient operator given by Formula (20).

Algorithm 3 Segmentation

Input: An entire 3D CT image CT **Output:** The 3D surface of the ossicles

- 1: Calculate each cubic area Ω of 3D CT image according to section 5.2
 - 2: $O = \text{SearchingOssicles}(\Omega)$
 - 3: **if** $O == \emptyset$ **then**
 - 4: There are no ossicles in this cubic
 - 5: **return**
 - 6: **end if**
 - 7: Calculate the signed distance function ϕ_0 , such that if $x \in \partial O$, $\phi_0(x) = 0$, if $x \in O - \partial O$, $\phi_0(x) > 0$, if $x \notin O$, $\phi_0(x) < 0$
 - 8: $i = 0$
 - 9: **repeat**
 - 10: $a = \phi_i^{-1}(0)$
 - 11: Update a using gradient descent of equation (18)
 - 12: Construct signed distance function ϕ_{i+1} in $|\phi_{i+1}| < \gamma$ using a
 - 13: $i = i + 1$
 - 14: **until** $\phi_i = \phi_{i-1}$
 - 15: Construct the zero isosurface of ϕ_{i+1}
-

result obtained based on Equation (20), i.e. using $G(x)$ to minimize the energy function (14). It is obviously that the ossicles should begin from the seventh image (although color is pale) or the eighth image in the figure. However, the detected result (Figure 10) starts from the ninth image. We show the magnified eighth image in Figure 11(a) and the pixels in red in Figure 11(b) belong to the ossicles.

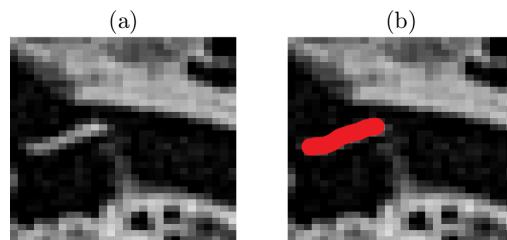


Figure 11. Ossicles’s localization in the eighth image in Figure 10.

Another classical approach to segmentation is the so called *snakes* or *active contours* method [23] [19], which is used as an effective local segmentation tool in most medical image processing software kits (see, e.g. [36]). Figure 12 is the segmentation result obtained by this method. Note that the result is not as good as result in Figure 10 since we only need to pay attention to the thirteenth thumbnail in Figure 12.

Figure 13 displays the result of segmentation obtained using our method, i.e. with Equation (6) as $G(x)$ to minimize the energy considered in Equation (14). The obtained result is clearly superior to the previous results by gradient operator or snakes method.

Next we visualize the reconstructed 3D ossicles. Generally speaking, there are two visualization method: One is to render a 2D projection of the 3D, such as volumetric ray casting [27, 35], the other is extracting isosurfaces (surfaces of equal values) from the volume and rendering them as polygonal meshes, such as marching cubes [6, 18]. Note that the signed distance $\phi(x)$ is an accurate and natural representation of ossicles, and $\phi^{-1}(0)$ is just right the boundary of ossicles. So we use marching cubes to generate the triangular mesh of *zero isosurface* of $\phi(x)$ to reconstruct the boundary surface of the ossicles. Figures 14 depict such surfaces obtained using gradient operator, Ricci curvature operator and snakes method, respectively. Apparently, the rendition in Figure 14(b) is the closest to the actual shape of ossicles than the ones in Figure 14(a) and Figure 14(c). We manually marked the shape of ossicles in this sample and constructed

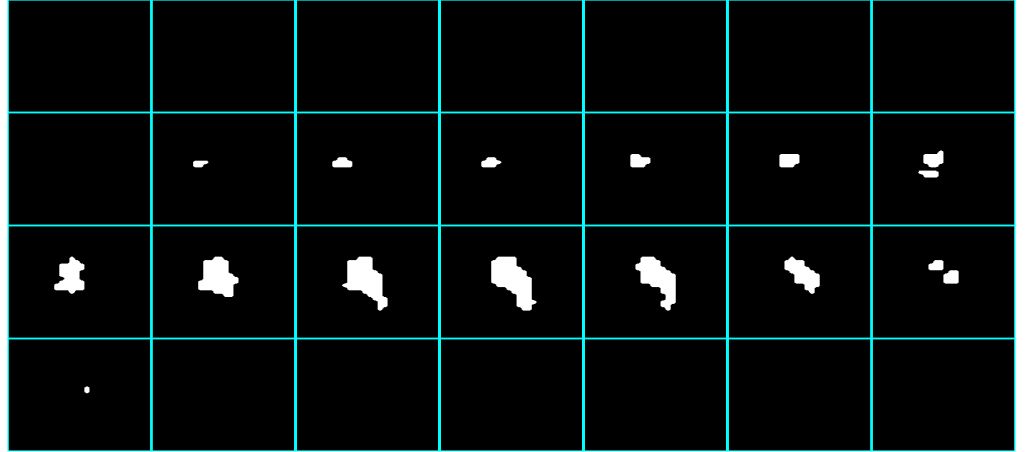


Figure 12. Segmentation results obtained using the snakes method.

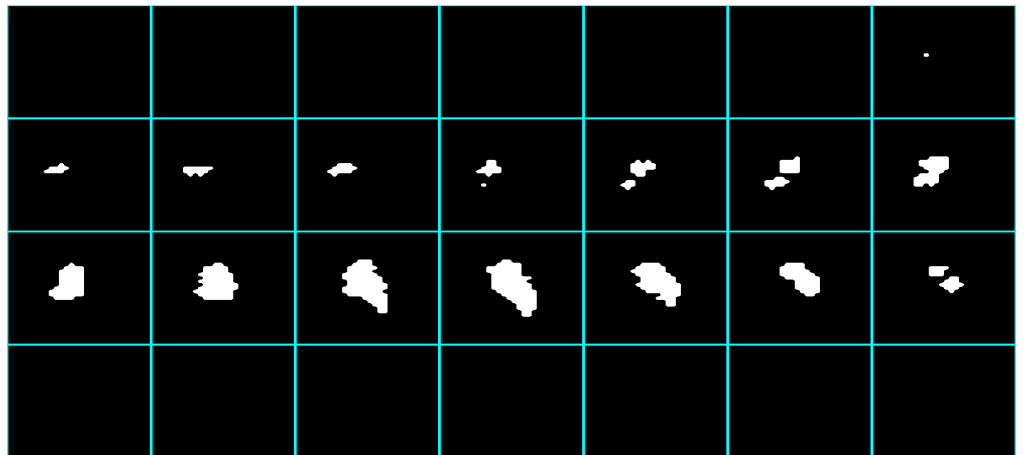


Figure 13. Segmentation results obtained using Ricci curvature.

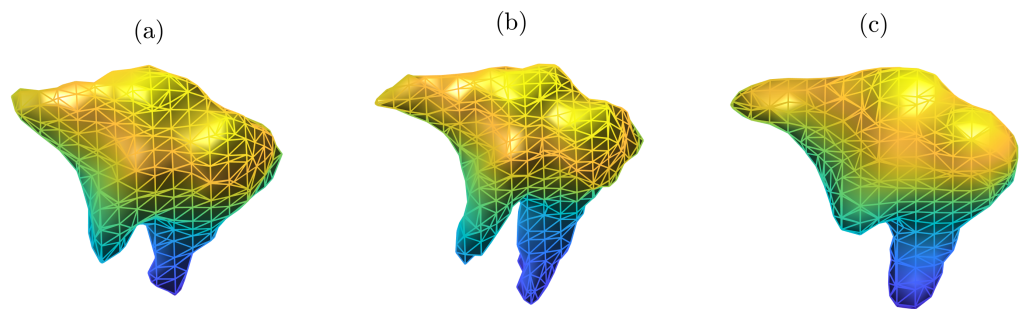


Figure 14. (a) The 3D ossicles' shape obtained using gradient operator (Equation (20)), (b) 3D ossicles' shape obtained using Ricci curvature, and (c) 3D ossicles' shape obtained using snakes method. Obviously, the two “legs” of the ossicles in (b) are longer than that in figure (a) and (c), which is closer to the accurate shape of ossicles. Thus Forman-Ricci curvature outperforms both the method based on gradient operator in Formula 20 and the one using snakes method.

the SDF (signed distance function) as the ground truth. Table 1 shows the deviations from the ground truth of various SDF's constructed employing different methods. It is clear that the proposed energy function with Ricci curvature operator derives the best result.

Table 1. Deviations from true SDF

Method	case 1 Deviation	case 3 Deviation
Snakes method	516.0106	$+\infty$
Energy function with $G(x)$ being gradient operator as Equation (20)	449.7176	394.3578
Energy function with $G(x)$ being Ricci curvature operator	24.2802	31.07

Note that the ossicles shown in Figure 9 are normal ossicles (Case 1). Next we show a more complicated case (Case 3). Figure 15 shows the 3D CT image region around the ossicles. As observed there is a substantial amount tissue fluid around the ossicles. This is the most complicated situation for segmentation. Figure 16 to Figure 18 shows the binary image of segmentation using the three method above. As we see, the snakes method produces a very error, as does Formula (20) has the same error as in the previous sample. We use the same parameter in these different case. Figure 19 represents the reconstructed surface of ossicles. Table 1 depict the deviations of these three method from ground truth. Obviously, Ricci curvature matches the real shape of ossicles very well.

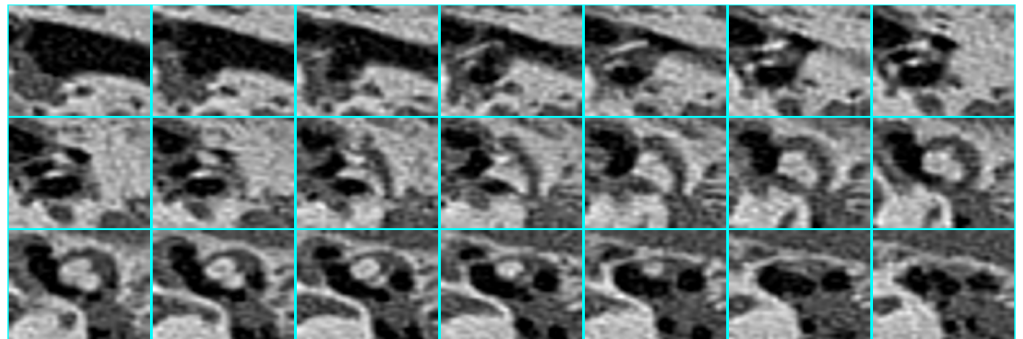


Figure 15. Ossicles surrounded by tissue fluid (Case 3).

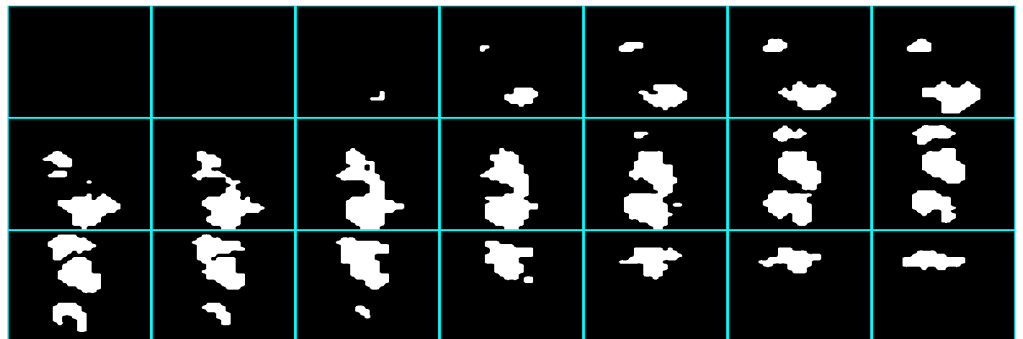


Figure 16. Segmentation result of Figure 15 using snakes method.

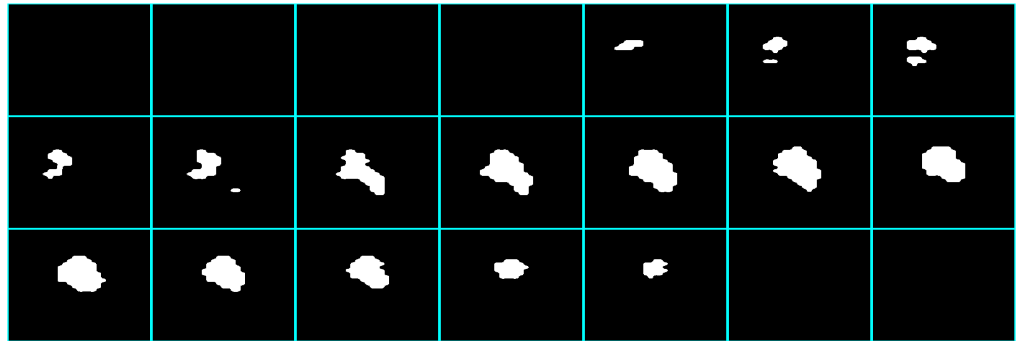


Figure 17. Segmentation result of Figure 15 using Equation (20).

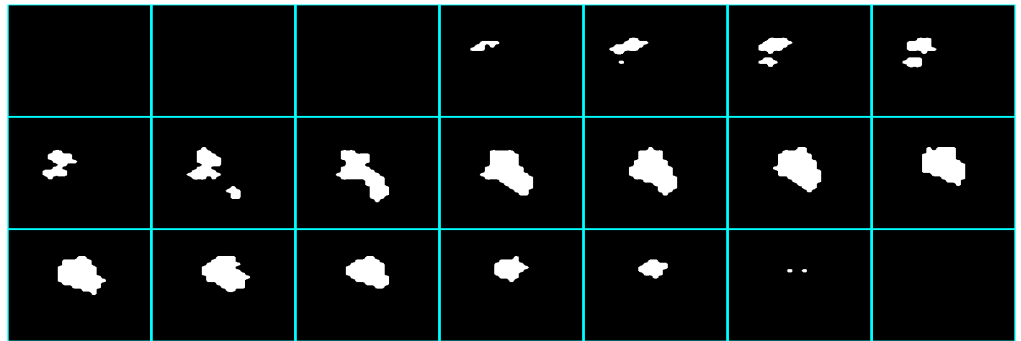


Figure 18. Segmentation result of Figure 15 using Ricci curvature.

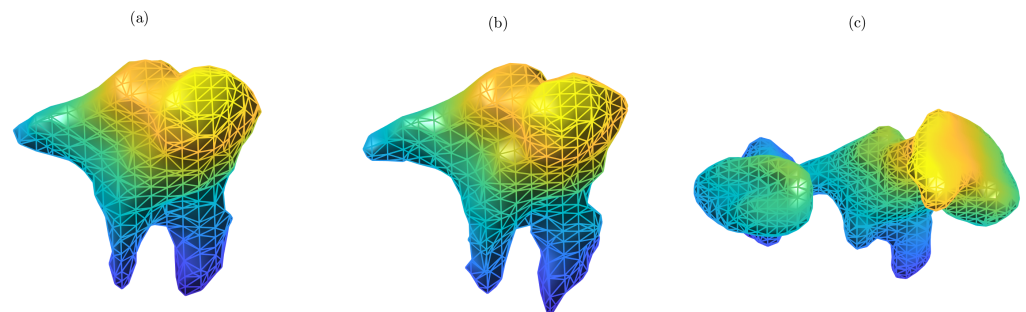


Figure 19. Reconstructed 3D Ossicles of Figure 15. (a) 3D ossicles' shape obtained using gradient operator (Equation (20)), (b) 3D ossicles' shape obtained using Ricci curvature, and (c) represents the 3D ossicles' shape obtained using the snakes method, which is far from complete due to the ossicles' connecting to the boundary.

9 Conclusion

This paper has two major contributions: First, a method for automatically positioning the ossicles is proposed, and secondly, the energy function with Ricci curvature is used to segment the 3D ossicles which be represented as triangular mesh. While curvature-based level sets represent the very core of Osher and Sethian’s original method [23], this paper shows that the the discrete Forman-Ricci curvature is highly suitable for segmenting small objects such as the ossicles, due to intrinsic edge detection capability of the curvature component. This edge detection capability of Forman’s Ricci curvature has already been demonstrated (see e.g. [29]). However, the Forman curvature used in the previous work cited above is the “full” (2-dimensional) version of the this curvature, which renders the computations more difficult than the extremely simple ones that make appeal to the graph version employed in the present paper. More importantly, the Forman-Ricci curvature of graphs allows us to concentrate on the main information contained in each pixel, without any averaging effect that may occur in the previously used 2-dimensional version. This is extremely important when dealing, like in the case of ossicles, with small groups of voxels (about 200 in our case). Furthermore, the Forman-Ricci curvature uses the voxel structure directly, without further processing, thus further enhancing its edge detection capabilities, especially on 3D image consisting of a small number of voxels.

10 Acknowledgments

This research was supported by the National Natural Science Foundation of China under Grant No. 61720106005, 61772105, 61936002 and 62041103.

References

1. N. Badshah and K. Chen. Multigrid method for the chan-vese model in variational segmentation. *Communications in Computational Physics*, 4(2):294–316, 2008.
2. J. A. Bærentzen. On the implementation of fast marching methods for 3d lattices. *Informatics and Mathematical Modelling*, 2001.
3. M. Berger. *A panoramic view of Riemannian geometry*. Springer Science & Business Media, 2012.
4. A. Chacon and A. Vladimirovsky. Fast two-scale methods for eikonal equations. *SIAM Journal on Scientific Computing*, 34(2):A547–A578, 2012.
5. B. Chow and F. Luo. Combinatorial ricci flows on surfaces. *Journal of Differential Geometry*, 63(1):97–129, 2003.
6. L. Custodio, T. Etienne, S. Pesco, and C. Silva. Practical considerations on marching cubes 33 topological correctness. *Computers & graphics*, 37(7):840–850, 2013.
7. H. Delingette. *Simplex meshes: a general representation for 3D shape reconstruction*. INRIA Sophia Antipolis, France, 1994.
8. J.-P. Eckmann and E. Moses. Curvature of co-links uncovers hidden thematic layers in the world wide web. *Proceedings of the national academy of sciences*, 99(9):5825–5829, 2002.

-
9. R. Forman. Bochner's method for cell complexes and combinatorial ricci curvature. *Discrete and Computational Geometry*, 29(3):323–374, 2003.
 10. J. Gao, X. David Gu, and F. Luo. Discrete ricci flow for geometric routing. In M.-Y. Kao, editor, *Encyclopedia of Algorithms*, pages 556–563. Springer New York, New York, NY, 2016.
 11. R. C. Gonzalez, R. E. Woods, and S. L. Eddins. *Digital image processing using MATLAB*. Pearson Education India, 2004.
 12. X. D. Gu and S.-T. Yau. *Computational conformal geometry*, volume 3. International Press of Boston Incorporated, 2008.
 13. R. S. Hamilton. The ricci flow on surfaces. In *Mathematics and general relativity, Proceedings of the AMS-IMS-SIAM Joint Summer Research Conference in the Mathematical Sciences on Mathematics in General Relativity, Univ. of California, Santa Cruz, California, 1986*, pages 237–262. Amer. Math. Soc., 1988.
 14. M.-Y. Kao. *Encyclopedia of algorithms*. Springer Science & Business Media, 2008.
 15. M. Kass, A. Witkin, and D. Terzopoulos. Snakes: Active contour models. *International journal of computer vision*, 1(4):321–331, 1988.
 16. M. E. Leventon, W. E. L. Grimson, and O. Faugeras. Statistical shape influence in geodesic active contours. In *5th IEEE EMBS International Summer School on Biomedical Imaging, 2002.*, pages 8–pp. IEEE, 2002.
 17. C. Li, C. Xu, C. Gui, and M. D. Fox. Distance regularized level set evolution and its application to image segmentation. *IEEE transactions on image processing*, 19(12):3243–3254, 2010.
 18. W. E. Lorensen and H. E. Cline. Marching cubes: A high resolution 3d surface construction algorithm. *ACM siggraph computer graphics*, 21(4):163–169, 1987.
 19. R. Malladi, J. A. Sethian, and B. C. Vemuri. Shape modeling with front propagation: A level set approach. *IEEE transactions on pattern analysis and machine intelligence*, 17(2):158–175, 1995.
 20. T. McInemey and D. Terzopoulos. Topology adaptive deformable surfaces for medical image volume segmentation. *IEEE transactions on medical imaging*, 18(10):840–850, 1999.
 21. D. Mumford and J. Shah. Optimal approximations by piecewise smooth functions and associated variational problems. *Comm. Pure Appl. Math.*, 42(5):577–685, 1989.
 22. Y. Ollivier. Ricci curvature of markov chains on metric spaces. *Journal of Functional Analysis*, 256(3):810–864, 2009.
 23. S. Osher and J. A. Sethian. Fronts propagating with curvature-dependent speed: algorithms based on hamilton-jacobi formulations. *Journal of computational physics*, 79(1):12–49, 1988.
 24. G. Perelman. The entropy formula for the ricci flow and its geometric applications. *arXiv preprint math/0211159*, 2002.
 25. G. Perelman. Ricci flow with surgery on three manifolds. *arXiv preprint math/0303109*, 2003.

-
26. K. M. Pohl et al. Logarithm odds maps for shape representation. In *International Conference on Medical Image Computing and Computer-assisted Intervention*, pages 955–963. Springer, 2006.
 27. S. D. Roth. Ray casting for modeling solids. *Computer graphics and image processing*, 18(2):109–144, 1982.
 28. E. Saucan and E. Appleboim. Curvature based clustering for dna microarray data analysis. In *Iberian Conference on Pattern Recognition and Image Analysis*, pages 405–412. Springer, 2005.
 29. E. Saucan, E. Appleboim, G. Wolansky, and Y. Y. Zeevi. Combinatorial ricci curvature and laplacians for image processing. In *Proceedings of CISP'09*, pages 992–997. IEEE, 2009.
 30. Y. Shavitt and T. Tankel. On the curvature of the internet and its usage for overlay construction and distance estimation. In *IEEE INFOCOM 2004*, volume 1. IEEE, 2004.
 31. R. Sreejith, K. Mohanraj, J. Jost, E. Saucan, and A. Samal. Forman curvature for complex networks. *Journal of Statistical Mechanics: Theory and Experiment*, 2016(6):063206, 2016.
 32. D. Terzopoulos, A. Witkin, and M. Kass. Constraints on deformable models: Recovering 3d shape and nonrigid motion. *Artificial intelligence*, 36(1):91–123, 1988.
 33. A. Tsai et al. A shape-based approach to the segmentation of medical imagery using level sets. *IEEE transactions on medical imaging*, 22(2):137–154, 2003.
 34. J. N. Tsitsiklis. Efficient algorithms for globally optimal trajectories. *IEEE Transactions on Automatic Control*, 40(9):1528–1538, 1995.
 35. D. Weiskopf. *GPU-based interactive visualization techniques*. Springer, 2007.
 36. P. A. Yushkevich et al. User-guided 3d active contour segmentation of anatomical structures: significantly improved efficiency and reliability. *Neuroimage*, 31(3):1116–1128, 2006.
 37. J. Zhang, K. Chen, and D. A. Gould. A fast algorithm for automatic segmentation and extraction of a single object by active surfaces. *International Journal of Computer Mathematics*, 92(6):1251–1274, 2015.
 38. M. Zhang, W. Zeng, R. Guo, F. Luo, and X. D. Gu. Survey on discrete surface ricci flow. *Journal of Computer Science and Technology*, 30(3):598–613, 2015.